Ocean Engineering 57 (2013) 83–98

Contents lists available at SciVerse ScienceDirect

Ocean Engineering

journal homepage: www.elsevier.com/locate/oceaneng

Spatial variability of ocean waves, from in-situ measurements

I.G.C. Ashton *, J-B. Saulnier, G.H. Smith

Renewable Energy Group, C.E.M.P.S., University of Exeter, Cornwall Campus, Treliever Rd, Penryn TR10 9EZ, United Kingdom

ARTICLE INFO

Article history:
Received 16 January 2012
Accepted 19 August 2012
Available online 16 October 2012

Keywords:
Wave measurement
Marine renewable energy
Resource assessment
Wave stationarity/homogeneity
Spatial variability of wave fields

ABSTRACT

This paper describes the analysis of the spatial properties of ocean waves using measurements from an array of four directional wave buoys installed in a square formation, with side 500 m, in the Celtic Sea, UK. Wave measurements in this area have been installed to support resource assessment and design for wave energy devices at the Wave Hub site off the North Cornwall coast. This unique deployment of multiple directional sensors provides high quality direct measurements of the spatial properties of the wave field. Spectral parameters measured simultaneously by all four buoys within the array are compared and it is demonstrated that wave conditions cannot be considered stationary across the measurement area. Differences in the measured wave fields were observed primarily in the low frequencies and are observed to be of a level sufficient to impact the assessment of site characteristics. Theoretical estimations of refraction and bottom friction indicate that these physical processes contribute to the observed measurements. The results demonstrate the potential effect of spatial variability in wave fields on the monitoring of wave energy sites, and highlight the requirement for accurate evaluation of physical processes.

1. Introduction

The development of devices to convert energy in ocean waves into electrical energy is underway throughout the world, with the aim of providing a meaningful contribution to global electricity supply. Leading technologies in this field are being deployed at sea at full-scale, either in designated test sites, or as commercial ventures. These early deployments are a critical opportunity for research and development of technology in real sea conditions. In order to maximise the benefits of a test deployment, accurate measurements of the physical conditions are essential to support analysis, and as such, test sites are often heavily instrumented. In addition to progression of the technology itself, test sites also offer an opportunity to develop procedures and strategies for the management of wave energy sites, including how wave conditions are monitored and assessed.

Published standards recommend that an active campaign of direct wave measurements at a wave energy site are combined with numerical modelling, to provide an accurate estimate of the long-term wave climate (Smith and Taylor, 2007; Pitt, 2009a). These data can be applied to estimate extreme conditions, and to assess the wave energy available at the site (Mollison, 1994, Pontes, 1996). Once a site becomes operational, direct measurements will also be used for the short-term analysis of device performance, and may be used to inform methods for monitoring the environmental impact of a wave farm (e.g. Millar et al., 2007).

However, spatial variability in wave conditions across the site has the potential to affect the accuracy of in-situ measurements. The practicalities of marine operations will commonly prohibit the deployment of instrumentation where a device is to be situated, particularly once devices have been deployed. For floating instruments, a safety margin will be required to prevent collision between wave energy converters (WEC) and wave sensors. A significant difference in the wave climate between a point of measurement and the location at which a device is to be situated will affect the assessment of the resource, and the performance of said device.

Best practice for the collection and analysis of wave measurements at a wave energy site has been the subject of significant research, and the results are published in the form of standards, or protocols. These have been developed in the UK to cover resource assessment (Smith and Taylor, 2007; Pitt, 2009a), and performance assessment (Pitt, 2009b), for wave energy. Furthermore, the EQUIMAR project reviewed standards for all aspects of data capture and analysis, and was developed from a European basis (Ingram et al., 2011) that will feed into the ongoing formation of international standards, through collaboration with the International Electrotechnical Commission (IEC). Each of these documents acknowledge the potential impact that spatial variability in the wave field will have on analysis for wave energy, and recommend that measurement locations are chosen to avoid systematic differences between measurement site and devices. Pitt (2009b) makes the specific recommendation for shallow

* Corresponding author. Tel.: +44 1326 254188.
E-mail addresses: I.G.C.Ashton@exeter.ac.uk (I.G.C. Ashton), J.Saulnier@exeter.ac.uk (J.-B. Saulnier), G.H.Smith@exeter.ac.uk (G.H. Smith).

0029-8018/$ - see front matter © 2012 Elsevier Ltd. All rights reserved.
http://dx.doi.org/10.1016/j.oceaneng.2012.08.010

water that where a difference in excess of 5% is predicted in the incident wave power, between measurement location and device location, a 'correction factor' should be derived for the power statistics applied to the device. A standard methodology for obtaining or applying this correction factor is not provided.

Despite the importance of spatial variability in wave conditions to the assessment of wave energy conversion, little direct data exists with which to examine the potential effect. Remote sensing technologies can provide spatial data sets for a wave energy site. However, the benefits of deploying multiple point measurements to describe spatial changes in the wave field are that the data collected are of excellent quality, with direct measurement of surface motions. As such, they are suitable for detailed analysis of wave processes across the area covered. Temporal resolution is also excellent, with continuous monitoring possible. When using floating wave buoys, spatial resolution is limited by the excursion radius of the device, which is commonly in the region of 50 m. Perhaps the greatest difficulty of such a system is that costs for deployment and servicing increase significantly when deploying multiple instruments offshore, relative to a single sensor.

In the past, multiple point measurements have been used for the intercomparison of wave sensors, and a review of this process is given in Krogstad et al. (1999). Such analysis commonly assumes that the wave processes are the same at all measurement points, or differences are negligible relative to the accuracy of the measurement process. An interesting example of such a project is the WADIC experiment (Allender et al., 1989), which compared the results from a variety of floating wave buoys, corroborated with other technologies and visual recordings. Sova and Wyatt (2005) used data from the WADIC experiment to compare simultaneous measurements in terms of the spatial variability of the wave field. Significant differences between data sets were primarily related to variability in wind fields affecting high-frequency waves. However, a key limitation of this study was that the measurements were derived from various sensors, and differences in their operation and performance could not be ruled out. More recently, two directional wave buoys have been installed at the European Marine Energy Centre (EMEC) wave energy test site, separated on similar scales of 500 m–2 km. Results from these buoys have been analysed for spatial variability and results indicate a significant difference in wave conditions across the EMEC test site (Smith et al., 2008; Barrett et al., 2009; Mackay, 2009).

This paper describes results obtained from a deployment of four directional wave buoys separated by 500 m, which is representative of the expected size of a wave energy test site. This deployment was conducted in an area close to the Wave Hub test site, Cornwall, UK, chosen such that the wave climate was broadly representative of that at a full-scale deployment site. Initial descriptions of the wave measurement site close to the Wave Hub wave energy test site in Cornwall, UK, and the instrumentation installed are provided in Section 1.1. Section 2 provides a review of the statistical analysis of wave data, and sampling variability associated with spectral estimates. Sections 2.2 and 2.3 describe the methods used for comparison of data between the data sets that were captured, before Section 3 provides results of the application of this analysis to spectral parameters and to spectral energy density in individual frequency bands.

1.1. The wave buoy array

During 2009 and 2010, four Fugro Oceanor SeaWatch mini II directional wave buoys were deployed by the University of Exeter, at a site close to the Wave Hub test site, Cornwall, UK (Fig. 1). The buoys were arranged in a square, with sides approximately 500 m.

A key upgrade made by Fugro Oceanor to the instruments that were supplied, was that the buoys are phase-locked so that measurements at each buoy co-incide. The clocks are synchronised with Co-ordinated Universal Time (UTC) via a GPS satellite receiver on each buoy, to an accuracy of ± 0.01 s.

The separation of 500 m between buoys was chosen as it is representative of the size of a single berth in the Wave Hub test site. It is also equivalent to the size of the safety zone imposed around the Wave Hub itself, within which marine operations, including the deployment of scientific instrumentation, are prohibited. As such, it corresponds to the likely minimum displacement of wave sensors from operating devices.

The deployment site is situated on the continental shelf of the UK, open to the Atlantic Ocean. As such, it has up to 6000 km of fetch and receives both swell and local wind waves from low pressure systems in the North Atlantic, which are more energetic during winter. Fetch from the northerly sector is limited to approximately 300 km by Ireland, which blocks swell propagation from the seas surrounding Iceland and Greenland.

The seabed at the deployment site is a mix of exposed bedrock and sandy gravel sediment. The bedrock protrudes approximately 8 m above the seabed, with depths in the site between 36 m and 46 m below chart datum (Fig. 2). This represents deep water for waves of wavelength below 72 m and 92 m ($f \sim 0.147$ and 0.130 Hz) respectively, and intermediate waters for all lower frequencies in the gravity wave spectrum. It follows that interactions between waves and the seabed can be expected to alter the properties of the wave field across the array.

Data for the tidal conditions at the site were extracted from the national tidal model, Polpred (POL, 2011). The model data provides estimates of tidal level, flow speed (integrated for depth) and direction, on a grid of resolution 500 m every 30 s. A grid output situated close to the centre of the buoy array, was taken to be representative of tidal conditions at all buoys. The tidal range is 5.8 m, inducing maximum currents of 1.2 m/s. Tidal flows are predominantly from the south west (230°) to the north east (50°) during a flood tide, and from the north east to the south west during an ebb tide.

Raw measurements of the water surface elevation were captured at a sampling frequency of 2 Hz for 1028 s (17 min 4 s) every 30 min, during a 13-month period between October 2009 and October 2010. Raw data were quality controlled in accordance with international guidelines for the analysis of oceanographic data (NOAA, 2005). Data processing was designed to follow the guidelines set out in Tucker (1993) and Tucker and Pitt (2001), in accordance with recommendations in Sanmuganathan (2009). Fig. 3 demonstrates the steps in data processing and the associated data returns at each stage.

For this research, comparing measurements between the wave buoys, it is critical that errors in the data set are minimised. Failure to do so will introduce inaccuracies on the same scale as the characteristics that are under investigation. Further confidence is gained through the limitation of all data sets to records where all buoys were measuring simultaneously and were error free. This process was seen to decrease the data available to less than the amount captured by the worst performing buoy. 16,320 records were available from the worst performing buoy position, although only 15,834 records made up the combined data set, which reduced to 14,673 after quality control.

An extended gap in the data during November and December 2009 occurred where the buoys were retrieved after a mooring failure (Fig. 4). This gap is during the more active winter months and although data are captured during 12 months, annual statistics such as the average power cannot be considered representative of

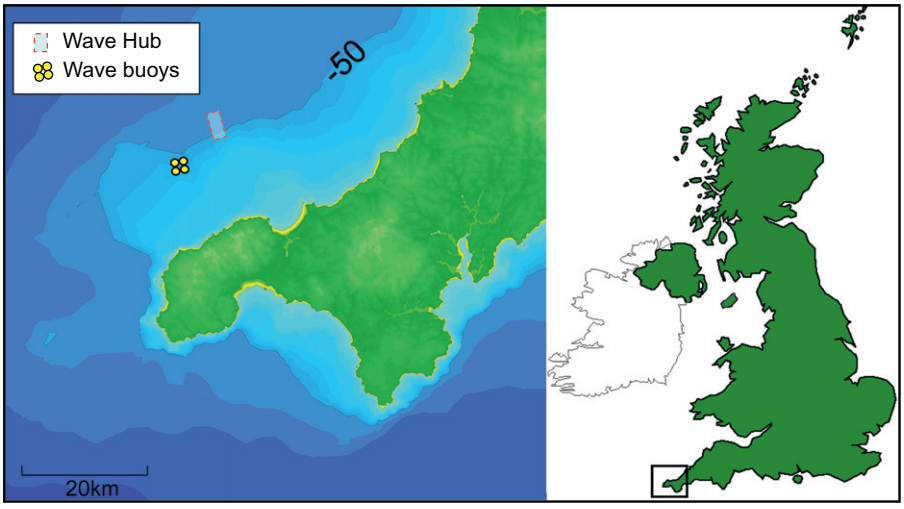

Fig. 1. The location of the wave buoy array.

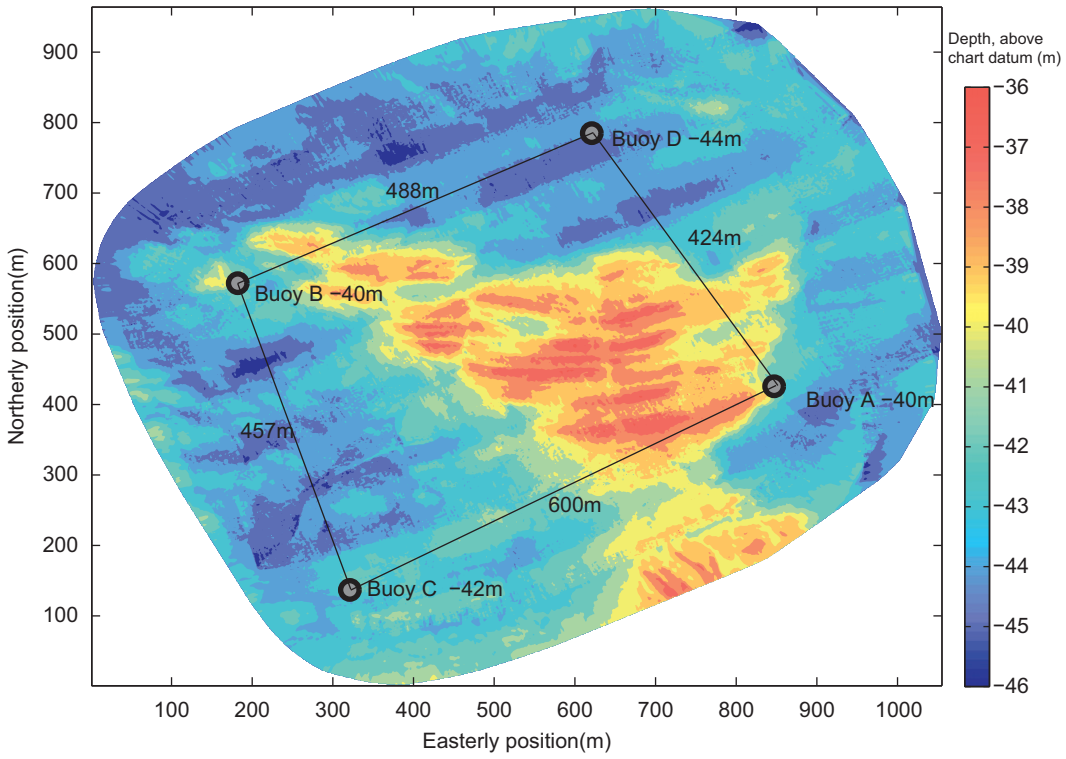

Fig. 2. The bathymetry at the wave buoy site, showing depths above chart datum. The four buoys are marked at their mean location, with the associated depths. The distances between buoys are also marked. Diagonal distances are 714 m (C:D) and 681 m (A:B).

the annual wave climate. A second gap appears during April, which was caused by battery failure in one buoy.

2. Statistical analysis of wave measurements

The buoys convert raw measurements of acceleration, heading and tilt into displacement time-series in three dimensions (vertical, east, north). Sampling frequency is 2 Hz and takes place during 1024 s (17 min 4 s), every 30 min, giving time-series with 2048 data points.

Spectral analysis was applied to decompose the time-series of surface elevation, $\eta(t)$, into N component regular waves of different frequencies, represented by a Fourier series as

$$\eta(t) = \sum_{i=1}^{N} [a_i \cos(2\pi f_i t) + b_i \sin(2\pi f_i t)] \quad (1)$$

The amplitudes a_i and b_i were calculated from the time-series for each Fourier harmonic using a FFT method, and the spectral variance density (periodogram) was calculated as

$$\hat{S}_j(f)\Delta f_j = \tfrac{1}{2}\sum_{i=1}^{k}(\hat{a}_i^2 + \hat{b}_i^2) \quad (2)$$

for $j=\{1,2,...,N\}$, where hats denote estimated quantities. Data were averaged over 8 frequencies ($k=8$), giving a variance density

spectrum for 128 individual frequency bands, between 0 and the Nyquist frequency (1 Hz), with resolution, $\Delta f = 0.0078$ Hz.

Spectral moments were calculated from the averaged, spectrum as

$$\hat{m}_n = \int_{f_1}^{f_2} f^n \hat{S}(f)\, df \tag{3}$$

where n represents the order of the spectral moment. Spectral filters removed data above f_2 and below f_1 to eliminate errors in the very high and very low frequencies. The limit $f_2 = 0.5$ Hz limit was set by the instrument manufacturer (Sanmuganathan, 2009). The low frequency filter, f_1, was 0.04 Hz, although an automated inspection of the variance spectrum was used to eliminate errors observed in the low frequencies (< 0.05 Hz). This process was used in response to specific low frequency errors, and full details can be found in Ashton (2011). Spectral moments were then used to calculate the significant wave height

$$H_{m0} = 4\sqrt{m_0} \tag{4}$$

and mean wave period

$$T_{m02} = \sqrt{\frac{m_0}{m_2}} \tag{5}$$

The dispersion equation (Eq. (6)) dictates that speed of propagation is dependent on the depth of the water, h, and the wavenumber, k. Hence, in intermediate or shallow waters, it is necessary to consider the speed of propagation of component waves when calculating wave power.

$$\omega^2 = gk \tanh kh \tag{6}$$

The phase velocity of the waves is given by

$$c_p = \left(\frac{g}{k} \tanh kh\right)^{1/2} \tag{7}$$

The group velocity is given by

$$c_g = \frac{1}{2} c_p \left(1 + \frac{2kh}{\sinh 2kh}\right) \tag{8}$$

In deep waters, wavenumber (and equivalently wavelength, $\lambda = 2\pi/k$) are solely dependent on wave frequency

$$\lambda_0 = \frac{gT^2}{2\pi} \tag{9}$$

As water depth decreases, wave frequency remains constant. At the point $(h/\lambda_0) \leq 0.5$, the dispersion relation (7) dictates that the wavelength will change with depth, however it cannot be solved for the wavelength directly. To approximate the true value the wavenumber, k, was calculated using an iterative procedure. The parameter h was estimated as the water depth for each location at mean tidal height. The incident wave power was then calculated as

$$P_t = \rho g \int_{f=0.04}^{f=0.5} c_g(f) \hat{S}(f) df \tag{10}$$

Process	Data returns
Measure data at 4 buoys	Over 13 months, servicing and failures cause gaps in the data. **89-93%**
Quality control	Alll data are quality controlled and errored records are removed **88 -91%**
Limit data to simultaneous records	Data limited to records where 4 buoys simultaneously return records that are error-free **80%**

Fig. 3. The data availability associated with each buoy, and how this is limited when data are restricted to records where 4 buoys were measuring simultaneously.

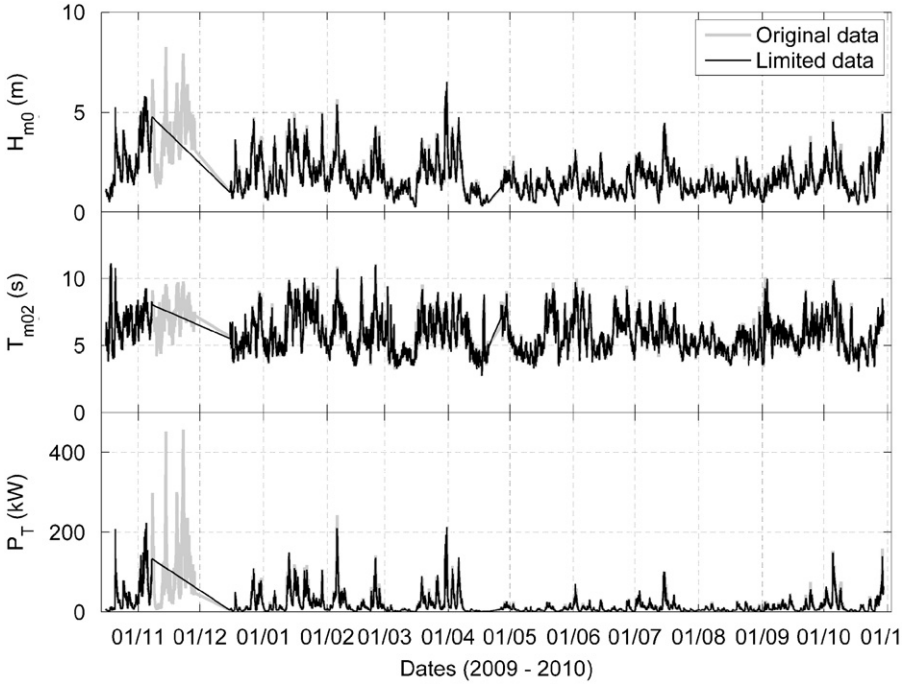

Fig. 4. Time-series of key parameters, H_{m0}, T_{m02} and P_t for buoy location B. The grey line shows the data collected, and the black line shows the limitations imposed by ensuring simultaneous data with the other buoys in the array.

P_t represents the total power per m wave crest, incident on the buoy from all directions.

2.1. Sampling variability in spectral estimates

Wave spectra, and spectral parameters are statistical summaries of a finite measurement of a continuous process (wave surface elevation). As a result, each parameter contains a random error component, and represents a value drawn at random from a distribution whose mean is the true value of that parameter in the sea state. In practice, the sea state may change during the sampling record, but for the purpose of analysis is assumed to be constant (temporal stationarity). Random variability can be described by the statistical distribution of parameter estimates about the mean (or true) value

$$\hat{X} = X + \varepsilon \tag{11}$$

where X denotes the true value of parameter, X, and ε is an error parameter drawn at random from a particular distribution. Statistical comparison between parameters requires a definition of this error distribution. The variance (error variance), or standard deviation (standard error) of this distribution are also used to describe the magnitude of random statistical variability in a given parameter estimate.

Eq. (2) expresses spectral estimates, $\hat{S}(f)$, as the sum of the squares of two Gaussian distributed random variables, which are known to follow a scaled Chi-Squared distribution. The degrees of freedom (which govern the magnitude of the error variance) are defined by the averaging used in spectral processing as (Tucker and Pitt, 2001)

$$\upsilon = 2p \tag{12}$$

where p is the number of averages used to derive $\hat{S}(f)$, in this case, $p=8$, $\upsilon=16$.

Krogstad et al. (1999) provides a definition of the covariance in spectral moments

$$cv(m_r m_s) = \frac{1}{D}\int_{f_1}^{f_2} f^{r+s} S^2(f) df \tag{13}$$

where m_r is a spectral moment of the order, r, and D is the duration of the record, in seconds. Setting $r=s$, this formula can be used to calculate the error variance in a spectral moment of the order r. Krogstad et al. (1999) go on to derive the following equations for the error variance in estimates of key wave parameters including H_{m0} and T_{m02} (Eqs. (4) and (5))

$$\sigma^2(\hat{H}_{m0}) = 4cv(m_0 m_0)/m_0$$

$$\sigma^2(\hat{T}_{m02}) = \frac{1}{4}\left(\frac{cv(m_0 m_0)}{m_0 m_2} - 2\frac{cv(m_0 m_2)}{m_2^2} + \frac{m_0 cv(m_2 m_2)}{m_2^3}\right) \tag{14}$$

where $\sigma^2(\hat{H}_{m0})$is the error variance of an individual estimate of H_{m0}. Spectral parameters are assumed to follow a Gaussian distribution about their mean (or true value for the sea state) and Eqs. (13) and (14) demonstrates that the variance will be dependent on the shape of the measured spectrum.

The classification of variability in spectral parameters requires quantification of the degrees of freedom in that parameter. Young (1986) shows that the effective degrees of freedom for a spectral parameter is not equivalent to the sum of the degrees of freedom for each spectral estimate, rather it is calculated as a weighted sum that depends on spectral shape

$$d.o.f. = \frac{\upsilon\left(\sum_1^N S_j(f)\right)^2}{\sum_1^N S_j{}^2(f)} \tag{15}$$

Elgar et al. (1987) demonstrate that when using discrete frequency bands, Eq. (15) will introduce a bias, which reduces with increasing averages. An equation to calculate this bias is given as

$$d.o.f._u = \frac{1}{1+(2/\upsilon)} d.o.f. \tag{16}$$

which shows that the maximum bias is a factor of 2, when $\upsilon=2$, and decreases as the number of averages is increased. By using both Eqs. (15) and (16), the number of effective degrees of freedom for spectral moments can be calculated.

2.2. Quantifying differences between summary parameters

Differences between wave conditions can be quantified in the first instance through the comparison of long-term mean values of summary parameters.

However, where simultaneous data are available, a more sensitive analysis can be achieved through comparison of data on a record by record basis using the proportional differences between measurements of a given parameter, from a pair of buoys, for a record, i as follows:

$$dX_i = \frac{X_{1i} - X_{2i}}{(1/2)(X_{1i} + X_{2i})} \tag{17}$$

where X_{1i} and X_{2i} are simultaneous measurements of a given parameter, X. This methodology was applied to $\hat{H}_{m0}$, $\hat{T}_{m02}$, $\hat{P}_t$ and $\hat{S}(f)$ data to calculate the proportional differences between simultaneous measurements.

Random variability in wave fields means that separate measurements of the same sea state will exhibit differences in the instantaneous or short term. However, the proportional differences, dX, would be expected to have a long-term mean of 0. The statistical properties of dX will be dependent on the sampling statistics of the parameter in question, X, which will vary on a record by record basis, and is dependent on the spectral shape of the underlying sea state (Eq. (13)).

Goda (1977) and Mackay (2009) express variability in measured data using the coefficient of variation (*c.o.v.*), which can be defined as follows:

$$c.o.v. = \frac{\sigma}{\mu} \tag{18}$$

This can be related to the proportional differences between two simultaneous measurements as

$$c.o.v. \approx \sqrt{2}\sigma(dX) \tag{19}$$

where $\sigma(dX)$ represents the standard deviation of the proportional differences of a generic parameter, dX. This formulation is used below to allow direct comparison with the literature (Goda, 1977; Mackay, 2009). Bias, or residual differences between the pairs of measurements, sampling variability, and any further sources of errors, such as instrument noise will affect this value.

The inclusion of theoretical predictions of sampling variability for each datum, allows calculation of the measured differences that are not explained by theoretical sampling variability. This important standardisation allows direct comparison of the measurement differences, or errors, from data sets measured in different wave climates.

Assuming the spectral parameter, X_i, to have a Gaussian error distribution, the difference between two independent values of X_i, will also be Gaussian distributed, with a variance equal to the sum of the error variances in the two contributing parameters. It follows that the standard error of the difference between two measurements of the same parameter, X_{1i} and X_{2i}, can be

calculated for a record, i

$$\sigma(\Delta X_i) = \sqrt{\sigma^2 X_{1i} + \sigma^2 X_{2i}} \tag{20}$$

where ΔX_i is the difference between X_{1i} and X_{2i}.

Sova and Wyatt (2005) use this formulation to derive a statistic, Z, that represents the ratio of the instantaneous differences between summary parameters and the theoretical standard error of that difference on a record by record basis

$$Z_i = \frac{X_{1i} - X_{2i}}{\sqrt{\sigma^2(X_{1i}) + \sigma^2(X_{2i})}} \tag{21}$$

where $\sigma^2(X_i)$ is the theoretical variance for a parameter calculated using Eq. (14). This formulation assumes independence between the two simultaneous estimates of X_i. Where this is not the case, a co-variance term must be included with the denominator in Eq. (21). For the purpose of this study, simultaneous measurements were assumed to be independent, although it is acknowledged that this may not be valid for all data.

The Z_i statistic was calculated using summary parameters for each pair of records in the data set. Where there is no difference between the underlying wave fields from which X_1 and X_2 were measured, the values of Z_i would be expected to follow a standard Gaussian distribution, with mean, $\mu Z = 0$, and standard deviation $sZ = 1$. If aggregated Z values do not have a mean of 0, the wave fields measured at the two points are not homogeneous. This was tested statistically using a two-tailed t-test with the null hypothesis, H_0, that there is no difference in the sea states at two measurement locations.

$$H_0 \rightarrow \mu Z = 0$$
$$H_1 \rightarrow \mu Z \neq 0 \tag{22}$$

A statistic, t, was calculated as

$$t = \frac{\mu Z - \mu}{sZ/\sqrt{n}} \tag{23}$$

where μ is the theoretical mean, and was set to 0, and n is the number of paired records. sZ was defined by the standard deviation of Z values. If $\mu Z = \mu = 0$, t will be a value from a Student's t distribution with $n-1$ degrees of freedom. The probability of a value drawn at random from the cumulative T distribution, with $n-1$ degrees of freedom, exceeding the calculated value for t, $p(t < T)$, was identified using look up tables. When $p(t < T)$ was below a critical threshold of 0.025, or above 0.975, H_0 was rejected and it was concluded that the differences in the wave field measured between two locations were significant to a 95% probability.

This methodology was applied to $\hat{H}_{m0}$, $\hat{T}_{m02}$and $\hat{P}_t$ estimates to assess the significance of observed differences between simultaneous data.

2.3. Quantifying differences between spectral estimates

In order to analyse the significance of observed differences between spectral energy densities at each frequency, $\hat{S}(f)$, it is more convenient to use the ratio of simultaneous measurements, $\hat{r}(f)$, defined as follows (Krogstad et al., 1999):

$$\hat{r}(f) = \frac{\hat{S}_2(f)}{\hat{S}_1(f)} \tag{24}$$

where $\hat{S}_1(f)$ represents the estimated spectral energy density, measured at location 1, for a given frequency band, centred on the frequency, f. Krogstad et al. (1999) also provide an unbiased estimator for $\hat{r}(f)$, with expected value of 1, as

$$\hat{r}_u(f) = \frac{\hat{S}_2(f)}{\hat{S}_1(f)} \frac{\upsilon_1 - 2}{\upsilon_1} \tag{25}$$

with variance

$$\sigma^2(\hat{r}_u(f)) = r^2(f) \frac{2(\upsilon_1 + \upsilon_2 - 2)}{\upsilon_2(\upsilon_1 - 4)} \tag{26}$$

Both $\hat{r}_u(f)$, and $\hat{r}(f)$ were calculated for each record, $i = \{1,2,3,...,n\}$, at each frequency, f. A long-term mean was calculated then calculated using

$$\bar{r}(f) = \frac{\sum_1^n \hat{r}_u(f)}{n} \tag{27}$$

where N is the number of records in the data set. Eq. (27) gives a mean spectral ratio at each frequency, $\bar{r}(f)$.

As described above, spectral estimates are chi-square distributed and the ratio $\hat{r}(f)$ will follow a scaled F distribution, with degrees of freedom defined by those of the spectral estimates (Eq. (15)). For these data, all spectral estimates have 16 degrees of freedom. Therefore, any value of $\hat{r}(f)$, would be expected to be drawn from the distribution, $F_{(16,16)}$, and, where the underlying wave states measured are the same, any combination of $\hat{r}(f)$ values would be expected to follow the distribution $F_{(16,16)}$ (where the unbiased ratio used, $\hat{r}_u(f)$, the F distribution would be scaled according to the second term on the RHS of Eq. (25)).

This assumption can form the basis for a hypothesis test, with the null hypothesis, H_0 that both samples are drawn from the same distribution, and therefore, that $\hat{r}(f)$values follow an F distribution

$$H_0 \rightarrow \hat{r}(f) \approx F_{(16,16)}$$
$$H_1 \rightarrow \hat{r}(f) \neq F_{(16,16)} \tag{28}$$

For an individual value, the probability that it was drawn from the appropriate distribution was calculated from the cumulative density function for the F distribution as $p(\hat{r}(f) < F)$. Where $p(\hat{r}(f) < F)$ was below a critical threshold of 0.05, or above 0.95, the null hypothesis was rejected with a confidence limit of 90%. For all 6 available pairs of buoy locations, this procedure was repeated for every record in the data set, giving a percentage of records for which the null hypothesis was retained. Based on the confidence limit set, this percentage has an expected value of 90%. Values below 90% indicate that for a given frequency, the differences between measurements from a pair of buoy locations cannot be explained by sampling variability alone.

3. Physical processes affecting wave propagation at the measurement site

The depth of the water at the measurement site is such that waves propagating across the site will be interacting with the seabed. In linear wave theory, waves for which, $(h/\lambda) \geq 0.5$ are considered deep water, as it is at this ratio that the seabed begins to influence wave processes. It follows that the interaction of waves and the seafloor at the site will only affect waves for which the deep water wavelength, $\lambda_0 \geq 76$ m. This relates to frequency components for which, $f \leq 0.143$ Hz. The interaction with the seafloor will increase with lower frequencies resulting in a complex pattern of energy loss and re-distribution throughout the measurement site. The key physical processes acting are, energy dissipation, which through bed friction will serve to remove energy from the waves, whilst refraction will alter the direction of wave crests and may focus or de-focus energy.

3.1. Bottom friction

Energy dissipation occurs through friction between the water column and the seabed in the boundary layer. Flows in the boundary layer are considered turbulent, and the energy dissipation due to

bottom friction, D_{bfr}, can be predicted as the time-averaged product of tangential shear stress and bottom velocity (see Holthuijsen (2007) for derivation).

$$D_{bfr} = -\rho C_{bfr} u_b^3 \tag{29}$$

where shear stress, $\tau_b = \rho C_{bfr} u_b^2$, $\rho = 1025$ kg/m^3 is the density of water, C_{bfr} is the bottom friction parameter, discussed below, and u_b is water velocity at the seabed. In the absence of ambient currents, the velocity at the seabed can be calculated using linear wave theory for a uniform periodic wave. For a regular periodic wave with angular frequency, ω, wavenumber, k and height, H, average energy dissipation per unit area per second becomes

$$\overline{D}_f = \rho C_{bfr} \left(\frac{\omega}{\sinh kh}\right)^3 \frac{H^3}{6\pi} \tag{30}$$

where the phase term in the velocity calculation is averaged over a wave cycle, $(1/2\pi)\int_0^{2\pi/\omega} \sin^3(\omega t)dt = 4/3\pi$. The metric used in this analysis was the proportional reduction in energy as it propagates across the site. This can be expressed as the ratio of energy removed to the energy contained in the original wave, $E = \rho g a^2$, giving

$$\Delta E_{bfr} = \frac{\overline{D}_f}{E} = \frac{2}{3\pi g} H C_{bfr} \left(\frac{\omega}{\sinh kh}\right)^3 \tag{31}$$

Notably, this formulation varies with H, showing that the energy lost through dissipation will rely on the frequency and the magnitude of the incoming wave train.

The constant, C_{bfr}, varies with the physical properties of the seabed. C_{bfr}, can be formulated in terms of the grain-size (or roughness) of the sediment, and Mirfenderesk and Young (2003) gives a comprehensive list of different formulations of which that of Madsen et al. (1988) is perhaps the most widely used. Wave induced bed formations will also affect C_{bfr}. Tolman (1994) describes a combined grain size and moveable bed model, the application of which requires detailed sediment data and consideration of the sediment regime beyond the scope of this paper. Bottom friction in the widely used spectral wave model, SWAN, can be formulated in terms of grain size (Booij et al., 1996). However, in the absence of detailed information about the seabed properties, a co-efficient that remains constant with the root mean square bottom velocity for all spectral components is commonly used, $C_{bfr} = x/gu_{rms}$ (Hasselman et al., 1973). x was originally defined as 0.038 m^2/s^3, although this is often considered applicable to swell conditions, and different values have been proposed for fully developed seas (Holthuijsen, 2007).

For this research, Eq. (31) was applied using a constant bottom friction parameter across the array, per frequency. This was applied to provide an estimate of the potential influence of bottom friction on wave energy propagating through the measurement site, to inform conclusions drawn from wave measurements. It was beyond the scope of this paper to attempt a detailed examination of sediment conditions in order to calculate an accurate estimation of wave conditions across the measurement array for incident sea states.

3.2. Refraction

Refraction of waves occurs when waves are slowed due to interactions with the sea-floor. This process can be predicted based on the linear model for propagation in finite water depth. The classic method is to plot a refraction diagram, which shows the propagation of wave rays, that begin as parallel lines, and bend according to the profile of wave crests. It is assumed that the energy flow between two rays remains constant. Therefore, changing their direction of propagation will concentrate or dissipate energy along the wave crest. The change in energy as a result of refraction can be quantified by the change in distance between wave rays. A shortening of the distance indicates a concentration of energy, whilst a widening of the gap indicates energy dissipation. Goda (2000) derives a coefficient of refraction, k_r, in terms of the change in wave heights for a regular wave

$$\frac{H}{H_0} = \sqrt{\frac{l_0}{l}} = k_r \tag{32}$$

For this research, the statistic of interest is the relative change in energy, which is equivalent to l_0/l, and here is denoted as ΔE_{rfr}.

Differences in the measured data will result from refraction of complex wave fields propagating from a range of different directions. For this research, a refraction diagram function was applied to calculate the effect of refraction on simple harmonic waves with frequencies centred on the frequency bands in the measured spectra, which was then repeated for waves propagating from a range of directions. The maximum changes in energy on the lee side of the measurement array were noted for each run, and represent the largest potential changes in wave energy affected by refraction on waves of different frequencies at this site.

Goda (2000) discusses refraction diagrams, and shows that the classic regular wave diagram will give inaccurate results for the case of a random, irregular sea. He demonstrates that when considering the combined effect of refraction in the whole spectrum, changes in wave height parameters (e.g. H_{m0}), are smoothed by the varying effect across the active frequency range. The quantification of refraction at individual frequencies described in this research paper, was used to demonstrate the potential impact of refraction on waves of varying frequencies at this site, and results will not be of equal magnitude when examining summary parameters.

3.3. Surface winds and tides

In addition to interactions with the seabed, tidal flows, and surface winds will interact with the surface wave fields. The influence of surface winds has been derived empirically for a standardised spectrum in the Jonswap experiment (Hasselman et al., 1973) and will predominantly transfer energy into the higher frequencies in the surface gravity wave spectrum. Wave-current interactions with tidal flows will alter the absolute propagation speed of waves of all frequencies. Similar to interactions of waves with varying seabed topography, tidal flow effects will cause energy bunching as waves get steeper, and refraction, which will alter the spatial distribution of energy across the measurement site. However, conversely to seabed effects, the effect of tidal flows will be proportionally greater on higher frequency waves.

For this experiment, ADCP flow meters were deployed to measure the current at the site. However, this provided a point measurement rather than a complete spatial analysis of current conditions, without which it is not possible to draw conclusions about the effects of ambient currents on the spatial distribution of wave conditions across the measurement site. It is acknowledged that the complex bathymetry may cause some spatial variability in the tidal flows. Without more data, it is not possible to predict whether this will have a significant effect on the short-term variability of the wave field, or long-term systematic differences in measurements across the array.

Wind conditions were not measured at the site, although in the absence of any nearby landmass, there seems to be justification in assuming that there is no systematic spatial differences in the wind field at the site. This would suggest that random variability in the wind field may increase variability in the high frequency waves, but not produce any difference in the long-term averages.

4. Results

Fig. 4 shows the time series of key spectral parameters, H_{m0}, T_{m02} and P_t, and demonstrates the wave conditions measured during the deployment. Measurements exhibited a close agreement between data from the four locations, although periods when they are not operational vary significantly between buoy locations. This reinforces the requirement for limiting the data to only records where 4 buoys were measuring simultaneously.

Table 1 The mean values of three key parameters at each location within the array

Parameter	Mean value at buoy			
	A	B	C	D
H_{m0} (m)	1.78	1.74	1.78	1.76
T_{m02} (s)	5.94	5.84	5.94	5.86
P_t (kW)	17.38	15.98	17.49	16.41

Table 2
The mean proportional differences in key parameters between pairs of buoys, expressed as a percentage.

Parameter	Mean proportional differences between buoys (%)					
	A:B	A:C	A:D	B:C	B:D	C:D
$\mu(dH_{m0})$	2.14	−0.06	1.09	−2.20	−1.06	1.15
$\mu(dT_{m02})$	1.46	0.03	1.25	−1.42	−2.1	1.22
$\mu(dP_t)$	5.76	−0.04	3.47	−5.80	−2.30	3.53

4.1. Consideration of average differences between summary parameters

The mean value of each of the key parameters are presented in Table 1. These values demonstrate differences between the data from different positions within the array with a maximum difference of 1.5 kW/m (9%) in the mean incident power measured between locations C and B. The differences between the other parameters were 0.05 m (2.6%) in H_{m0}, and 0.09 s (1.6%) in T_{m02}.

4.2. Record by record differences between summary parameters

The proportional differences in the key parameters between locations were calculated on a record by record basis using Eq. (17), giving three data sets of differences for each pair, dH_{m0}, dT_{m02} and dP_t (Table 2).

P_t again exhibits the largest mean difference between pairs, which is greatest at −5.8% between locations B and C, and smallest at −0.04% between locations A and C. However, the maximum difference of −2.1% occurs for the parameter T_{m02}, between the pair, B and D (Table 2).

The *c.o.v.* values, calculated using Eq. (19) were seen to be consistent across all pairs, and had mean values of 5.2%, 3.2%, and 12.42% for of H_{m0}, T_{m02} and P_t respectively. These values agree closely with Mackay (2009), who calculated the *c.o.v.* of H_{m0} and T_{m02} estimates, from a single pair of buoys, separated by 1500 m at the EMEC site to be 6.2% and 4.5% respectively.

The time series of dH_{m0}, dT_{m02} and dP_t for a single pair of buoy locations are presented in Fig. 5. These graphs demonstrate periods over which the parameters persistently deviate from a zero mean, which is not consistent with the assumption that sampling variability the sole reason for observed differences

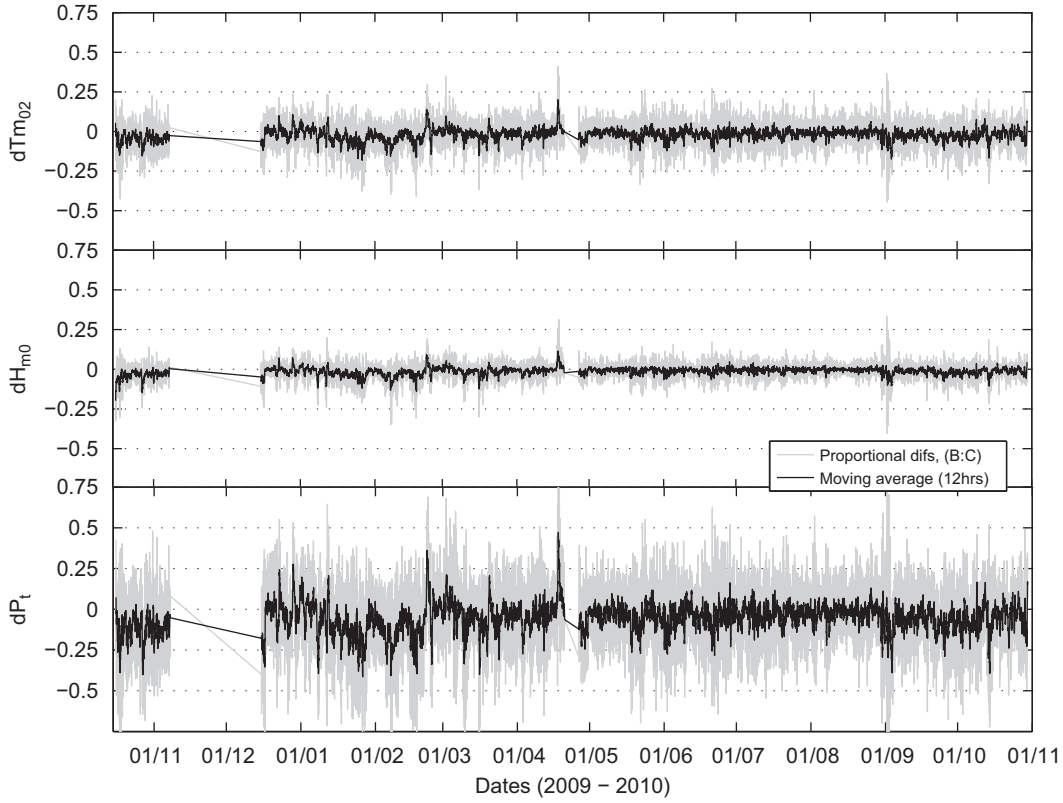

Fig. 5. Proportional differences between locations B and C for the three key parameters, dH_{m0}, dT_{m02} and dP_t calculated using Eq. (12). Also shown is a moving average of each parameter, taken over 12 consecutive records.

(Fig. 5). Key examples include the first period of deployment, October and November 2009, during which the proportional differences between measurements at locations B and C were persistently less than 0, for each parameter. These differences are again greatest in P_t, and during 4 weeks, the mean difference was −12.41%. A second period where measurements at location B are consistently less than at location C can be identified during January and February 2010, contributing to an average difference of −14.0% between the 14 January and the 20 February 2010.

The differences presented in Fig. 5 are for the pair B:C, and are of the largest magnitude in terms of the parameter dP_t. However, other pairs demonstrate the same temporal properties, of a different scale, which suggests the same underlying causes affecting spatial differences between all measurements.

In order to establish the statistical significance of observed differences between summary parameters, a set of Z statistics were calculated for each pair of buoys for the three key parameters using Eq. (21). The mean of the Z statistics ranged from 0.00 to 0.38 (absolute values). Notably, the largest values were consistently attributed to the T_{m02} parameter, and values for the pairs B:C and A:B were the largest for all parameters. The associated t values were also calculated using Eq. (23) and for most records, the mean of the Z statistic was found to be significantly different from 0. This indicates that differences in measurements of these parameters across the site are significant to a 95% probability. The two exceptions to this result occur for the pair of measurements at locations A and C where the mean Z statistic for H_{m0} was small, $\mu Z(H_{m0})=0.001$ (for which, $t=0.11$ and $p=0.9$). Therefore, the null hypothesis was retained, and the differences were not deemed significant. This was also the case for the wave power measurements, $\mu Z(P_t)=0.014$ with $t=1.7$ and $p=0.09$. In contrast, for wave period measurements at locations A and C, $\mu Z(T_{m02})=0.050$, which was deemed to be significant.

In all but one case, the standard deviation of the Z statistic is greater than 1, with the highest value, $\sigma Z(T_{m02})=1.15$ occurring for the pair B:C. This indicates that the variability in measured data is greater than that predicted by sampling theory alone. The exception is the result for incident wave power, $\sigma Z(P_t)=0.98$, for the pair B:D, which indicates that the variability between these measurements is less than that predicted by sampling theory. In contrast to the mean values, μZ, the standard deviations, σZ, were consistently smallest for P_t, and greatest for T_{m02}. Variability between estimates of the parameter P_t are within, or close to the levels predicted by sampling theory, whereas the estimates for other parameters are not. Furthermore, whilst results in Tables 1 and 2 indicate that bias has the greatest effect on P_t, analysis of the Z statistics shows that measurements differences are greatest in the parameter T_{m02}, relative to sampling variability.

4.3. Record by record differences in spectral estimates

Spectral analysis of the raw time-series provided n variance density spectra, with 128 discrete frequency bands, for the 6 pairs of buoy location data sets within the array (where n is the number of records in the data set).

The proportional differences between spectral estimates, $\hat{S}(f)$, at each of the 128 discrete frequency bands in variance spectra, were calculated on a record by record basis using Eq. (17). The results provide n values of the parameter,$d\hat{S}(f)$, for each pair of buoy locations in the array. The mean values, $d\bar{S}(f)$, plotted in Fig. 6, reveal that the largest mean proportional differences between locations occur in the low frequency measurements for all pairs.

The greatest proportional differences were between estimates for locations A and B, which reached 11.25% at 0.07 Hz ($T=13.5$ s). Reflecting the results for parameters, some variability in the magnitude of the observed differences was observed for different pairs. Pairs A:C and B:D showed notably smaller differences in the low frequencies than the other pairs. However, for all pairs, differences were seen to increase for estimates of frequencies below 0.13 Hz. An increase in mean differences was also observed for high frequencies, and at the 0.5 Hz frequency cut-off used for parameter estimation, the maximum difference was 4% between locations C and D.

Notably, the pair A:B exhibited the greatest difference in the low frequencies and the least difference in the high frequencies. This explains results in Table 2 where the pairs exhibiting the greatest differences between parameters was not the same for P_t,

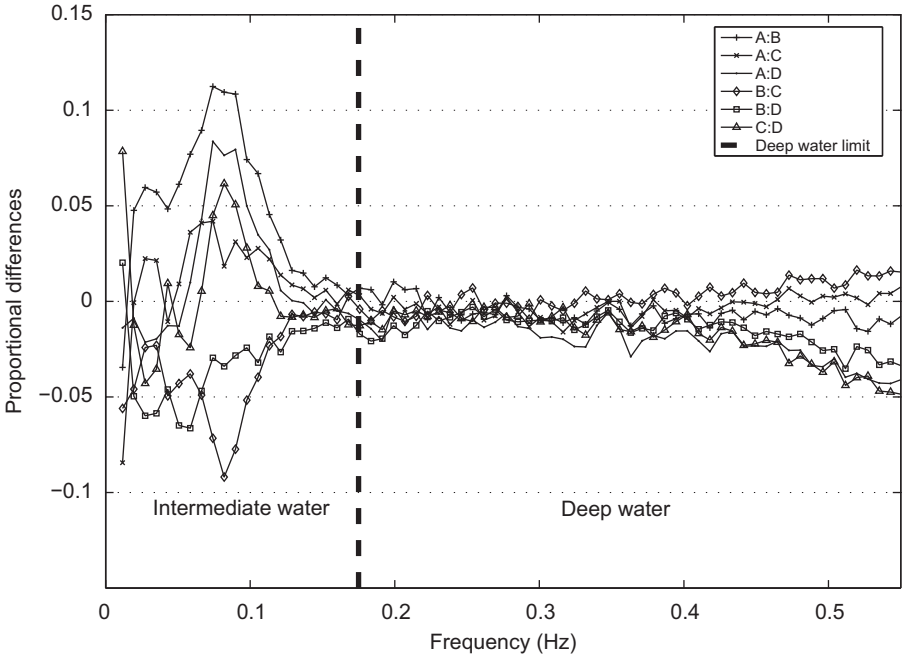

Fig. 6. The mean proportional difference between spectral energy density at each frequency band, for pairs of buoys.

which is strongly dependent on low frequencies, and T_{m02}, which is more dependent on high frequencies through its inclusion of m_2 (Eq. (5)).

For each pair of locations, the spectral ratio, $\hat{r}_u(f)$, was calculated using Eq. (25), and the mean value was found using Eq. (27), to provide an unbiased estimator of the ratio between variance density spectra. Fig. 7 displays the calculated values of $\bar{r}(f)$ for each pair of locations in the array. Values at frequencies below 0.1 Hz increase rapidly with lower frequencies and below 0.07 Hz, are orders of magnitude different than 1, reflecting the large differences indicated in Fig. 6. For clarity, very large values at low frequencies are not shown on Fig. 7. Across the range of frequencies 0.15–0.4 Hz, $\bar{r}(f)$ is consistently close to 1. There is some variation between the pairs, and within this frequency range, the pair B:C exhibits values closest to 1, despite demonstrating the largest differences between spectral parameters (Table 2).

The standard deviation of the spectral ratio, $\sigma^2(\hat{r}_u(f))$, was calculated using Eq. (26), to have an expected value, $E[\sigma(r)]=0.56$ for all frequencies. Variability in low and high frequencies causes large values of $\sigma^2(\hat{r}_u(f))$ below 0.1 Hz and above 0.35 Hz. However, over the central frequency range, the standard deviations of the measured data are close to this value (Fig. 8). This demonstrates that theoretical sampling variability is suitable to explain differences in the measured data. Within this range, the variability can be seen to decrease at lower frequencies, potentially due to increasing correlation between the wave records.

The hypothesis test, on the ratio, $\hat{r}_i(f)$, calculated using Eq. (24) for the n records in the data set was applied with a 90% significance level and the results are shown in Fig. 9. In the frequency range, $0.13<f<0.4$ Hz, the null hypothesis, H_0 was retained for approximately 90% of values. This result demonstrates that for these frequencies, the ratio between simultaneous estimates follows an F distribution with appropriate degrees of freedom, and supports previous results that measurements in this region are consistent across the four data sets. For higher frequencies, $f>0.4$ Hz, a decrease in the proportion of records retaining the null hypothesis was observed, which can be attributed to the influence of the bias (Figs. 6 and 7) and increased variability at higher frequencies (Fig. 8). For three pairs, A:C, B:D and C:D, more than 90% of records retained the null hypothesis for frequencies, $0.1<f<0.13$ Hz. This indicates that measured differences between spectral estimates at these frequencies are less than predicted due to theoretical sampling variability. This is potentially due to correlation in the underlying time-series, which would be expected to primarily affect low frequencies.

Results displayed in Fig. 9 for frequencies below 0.1 Hz, reflect those in Figs. 6 and 7, with a dramatic decrease in the proportion of records retaining the null hypothesis with frequency.

5. The influence of physical processes

To aid conclusions relating to the observed differences in measured data across the array, this section estimates the potential contribution of physical processes on the wave field. The cumulative effect of two key source terms, bottom friction (Eq. (31)), and refraction (Eq. (32)), were calculated for the same frequency bands that were estimated in the measured wave spectra. This was based on the bathymetry data plotted in Fig. 2. The aim of this study was not to predict the measured differences described in Section 4. Rather, it was to predict the potential impact of these source terms, and their frequency distribution, in order to establish whether they are of a similar magnitude to the observed differences.

5.1. Bottom dissipation

In order to predict the potential influence of energy dissipation through bottom friction, the drag-flow model described by Eq. (29) above, was applied to calculate the cumulative energy loss due to bottom friction across the measurement array. This was achieved by calculating the cumulative energy loss for each metre in the direction of travel of the waves for the range of frequencies measured by the buoys, $0.04\leq f\leq 0.5$ Hz, using Eq. (30). A constant bottom friction co-efficient with value 0.01 was used, which represents an approximation, albeit one that is commonly used as a default value for large-scale wave models (Tucker and Pitt,

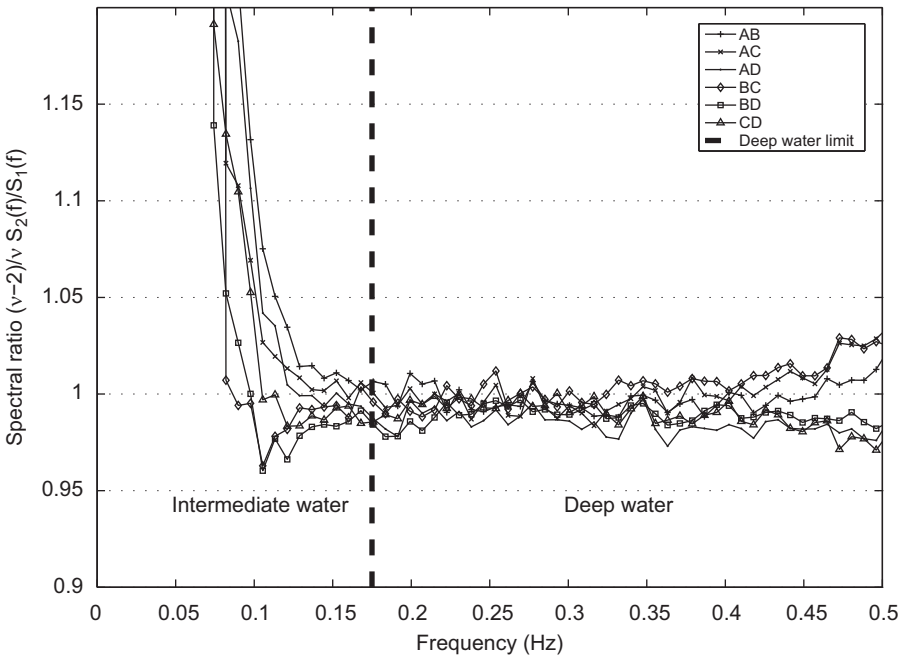

Fig. 7. The mean spectral ratio, μr, for each pair of buoys.

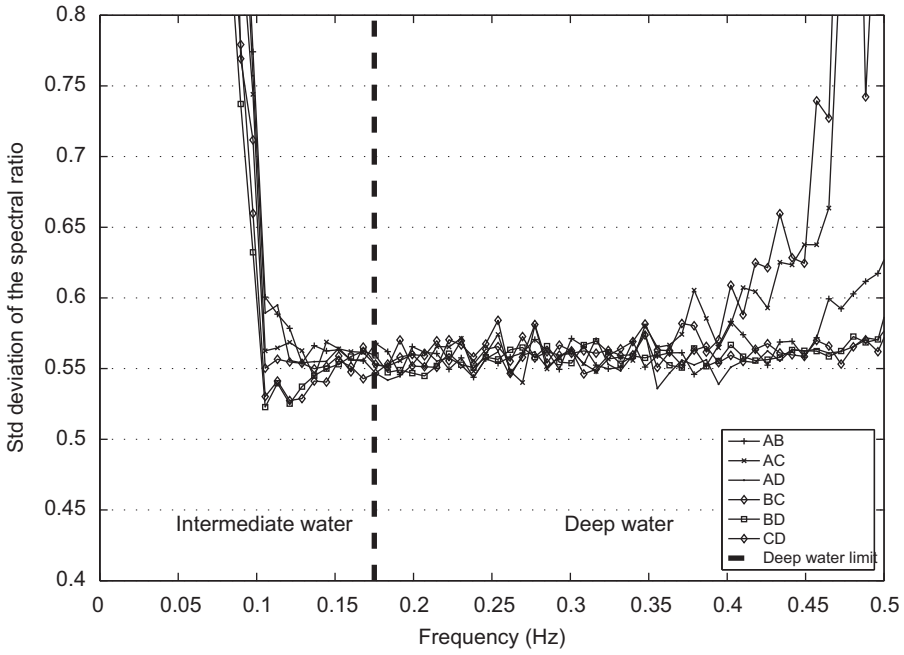

Fig. 8. The standard deviation of the spectral ratio, $\hat{r}(f)$, for each pair of buoys.

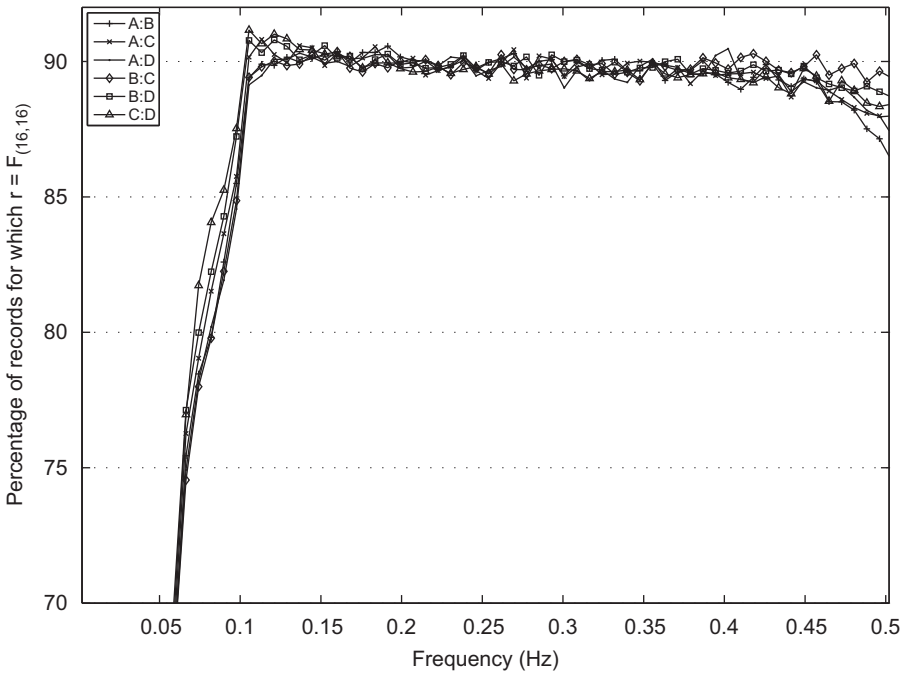

Fig. 9. The percentage of records for which the spectral ratio, $\hat{r}_i(f)$, was deemed to be drawn from the distribution $F_{(16,16)}$, by a hypothesis test with 90% significance level, for each frequency band in the wave spectrum.

2001). Results were calculated as the proportional difference between an eastern boundary, a north–south line passing through the location of buoy B, and a western boundary, a similar line passing through the location of buoy A in Fig. 2. Locations with no bathymetry data were represented with a constant value of −44 m. This will render the most northerly and most southerly values inaccurate, due to the limited bathymetry for these transects (Fig. 2).

Fig. 10 shows the proportional energy dissipated, per frequency, for waves of varying frequency, but constant energy ($H=1$), propagating through the array from west to east. An increase of the effect of bottom friction with decreasing frequency can be observed, demonstrating the increased potential for energy dissipation in waves of lower frequency and longer wavelength. However, energy dissipation is also dependent on the initial energy in the wave train. Therefore, for comparison with the measured data, it is important to take into account the levels of energy that can be experienced at this site, for waves of different frequencies.

The proportional energy dissipation was also calculated using H values defined for each frequency band to represent a regular wave with the same energy as the measured mean (Fig. 11) and max (Fig. 12) spectral energy density values in the data

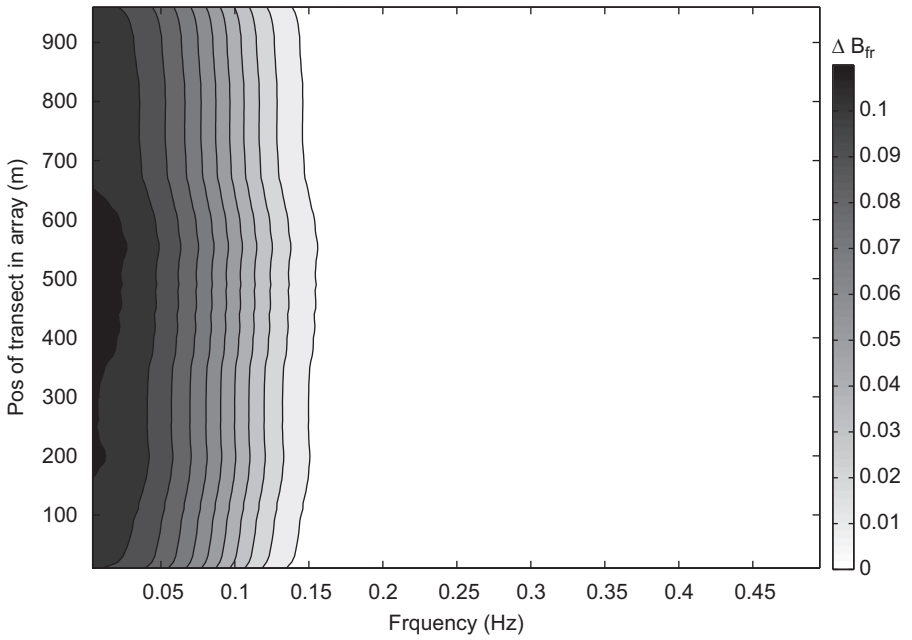

Fig. 10. The proportional difference in spectral energy due to bottom friction as waves propagate through the array. The energy associated with each frequency band is constant.

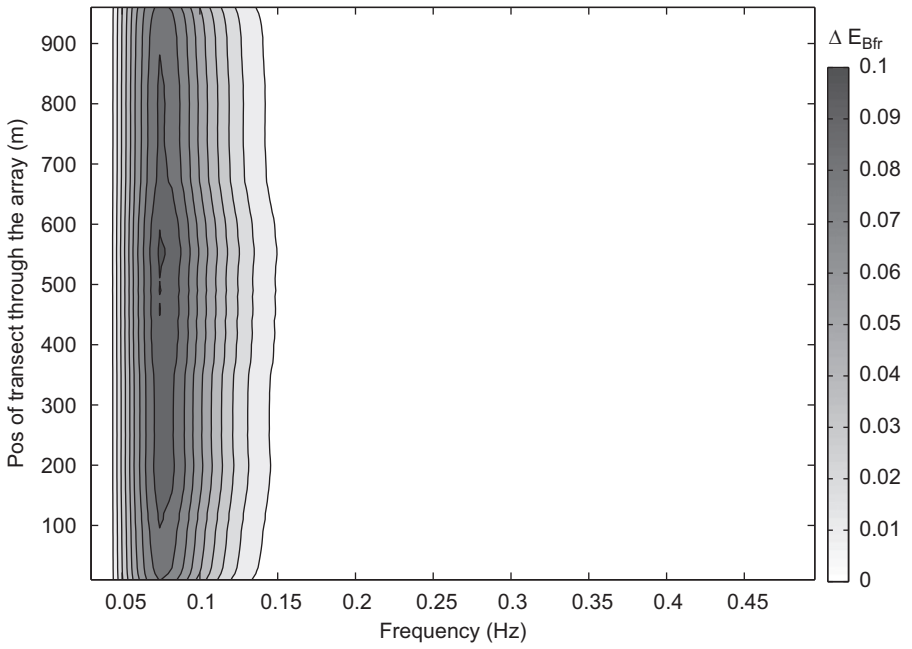

Fig. 11. The proportional difference in energy due to bottom friction as waves propagate through the array in a westerly direction. The initial energy within each frequency band is equal to the mean spectral energy measured at the Northerly position in the array, and the co-efficient, C_{bfr}, was set to 0.01.

measured at the westerly position (buoy B). The magnitude of the observed proportional differences reached a maximum of 11% for the mean case, increasing to 42% for the maximum energy per frequency. The dependency on frequency observed in Fig. 10 is tempered by the dependency on the initial energy for individual components.

Through examination of the maximum difference per frequency for all transects through the array (Figs. 13 and 14), it is observed that the difference in energy exceeds 1% for frequencies, $0.04 \leq f \leq 0.15$ Hz, both for mean (Fig. 13), and maximum (Fig. 14) spectral values. This can be compared with results presented in Figs. 6 and 7, where significant differences in the spectral estimates were observed at these frequencies.

5.2. Refraction

A refraction diagram was plotted for the centre of each frequency band in the measured spectra. Fig. 15 gives an example refraction diagram, for a simple harmonic wave of frequency 0.066 Hz, with an initial direction from west to east. The maximum changes in energy on the lee side of the measurement array, along a line orientated north–south level with buoy A, were noted for

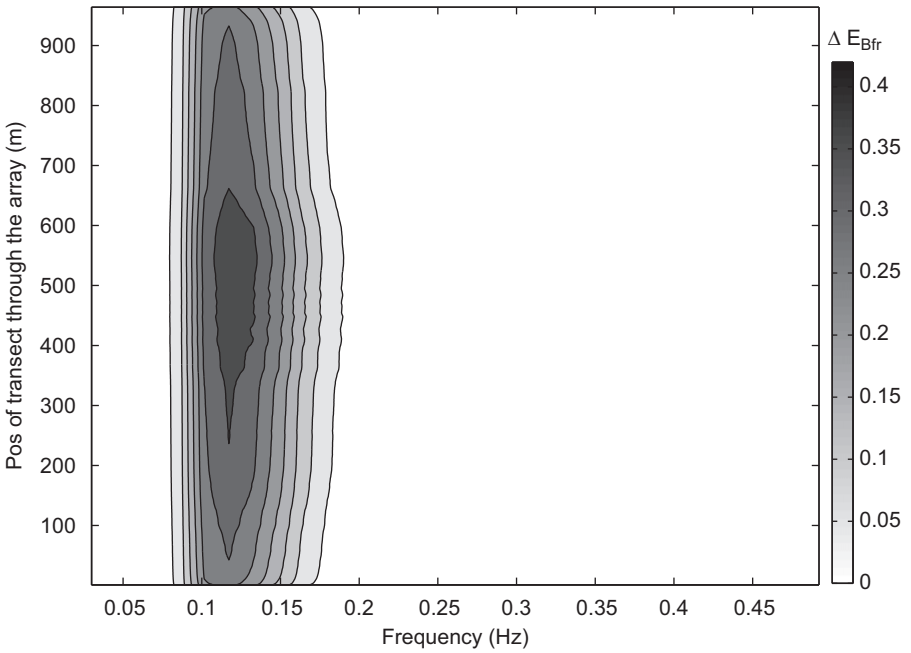

Fig. 12. The proportional difference in energy due to bottom friction as waves propagate through the array in a westerly direction. The initial energy within each frequency band is equal to the maximum spectral energy measured at the Northerly position in the array, and the co-efficient C_{bfr} was set to 0.01.

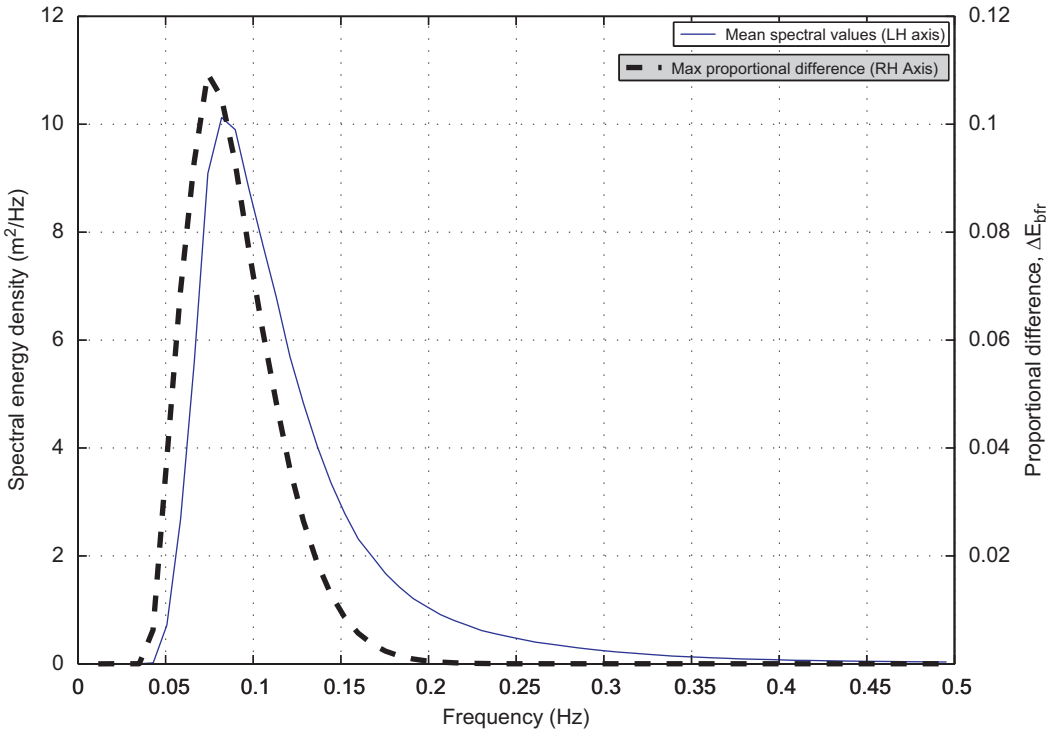

Fig. 13. The maximum proportional difference in energy due to bottom friction, of all transects through the array in a westerly direction (RH axis). The co-efficient C_{bfr} was set to 0.01, and the initial energy in each frequency band is equal to the mean spectral energy density measured at the northerly position within the array, also plotted (LH axis).

each frequency, $\max(\Delta E_{rfr}(f))$, and represent the largest potential changes in wave energy due to refraction, on waves of different frequencies, propagating in this direction (Fig. 16). Differences are observed for frequencies below 0.15, although they do not increase consistently with lower frequencies.

Refraction will be dependent on the direction of propagation, which was assessed through calculating $\max(\Delta E_{rfr}(f))$ for 10 separate directions of propagation, spread evenly between 0° and 360°. The average maximum change in energy due to refraction, $\max(\Delta E_{rfr}(f))$, exceeds 1% only for frequencies below 0.15 Hz. It was also seen to increase with a decrease in wave frequency (Fig. 16). The maximum values provided here are indicative of the potential for re-distribution of wave energy. However, their definition as the maximum change across the array, means that their magnitude cannot be compared directly to the measured values.

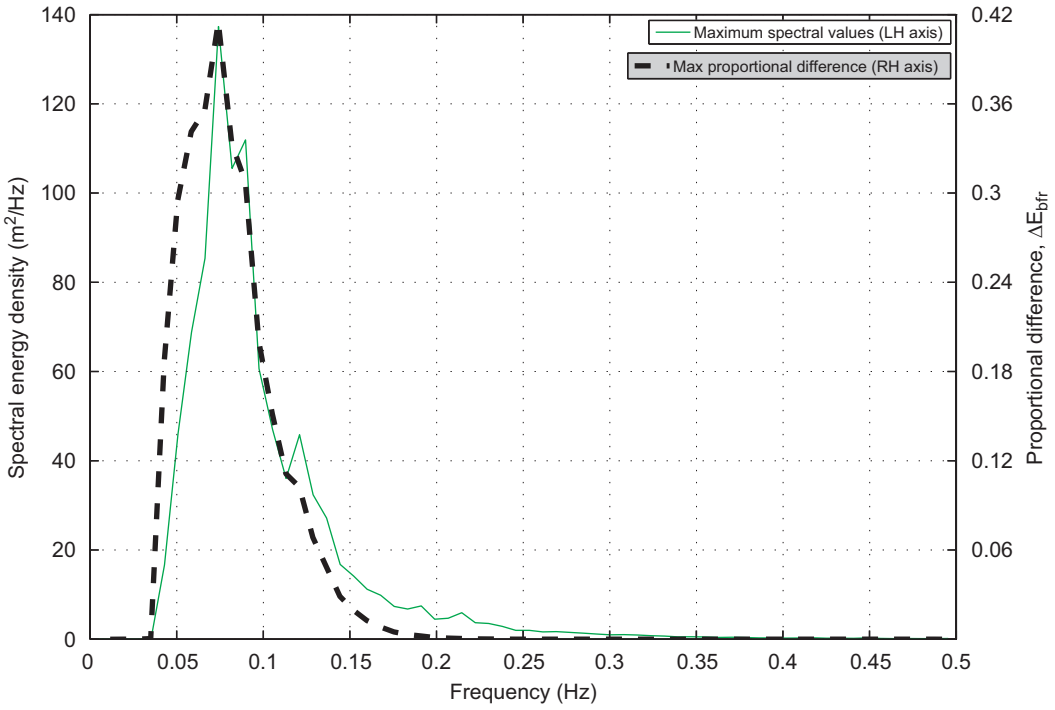

Fig. 14. The maximum proportional difference in energy due to bottom friction, of all transects through the array in a westerly direction (RH axis). The co-efficient C_{bfr} was set to 0.01, and the initial energy in each frequency band is equal to the maximum spectral energy density measured at the northerly position within the array, also plotted (LH axis).

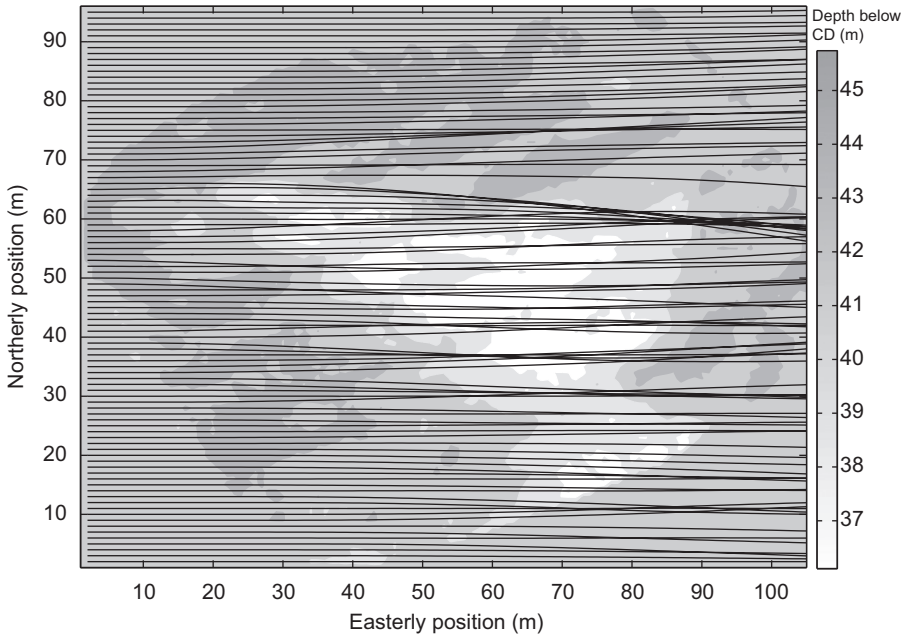

Fig. 15. An example refraction diagram, for a simple harmonic wave of frequency 0.066 Hz, with an initial wave direction from west to east.

6. Discussion

A unique deployment of four time-synchronised, directional wave buoys has been used to analyse the spatial properties of ocean wave fields on the scale of proposed wave energy arrays, or wave farms. A detailed statistical investigation demonstrates that key parameters vary significantly between the data sets. Quantifying the observed differences in terms of the theoretical variability for each datum provides a robust assessment of the measured data. The methodology presented is recommended for future analysis of similar data sets, as it ensures that results are directly comparable between data sets of different wave conditions, captured from different sites or measurement periods. Inclusion of this analysis in a resource assessment would make results more robust, and provides critical information for subsequent performance assessments at site.

Of the parameters compared, the measured differences were greatest for the mean incident wave power, where an 8.6% difference was observed for 12 months of data. This parameter is critical for resource assessment of a proposed wave energy site,

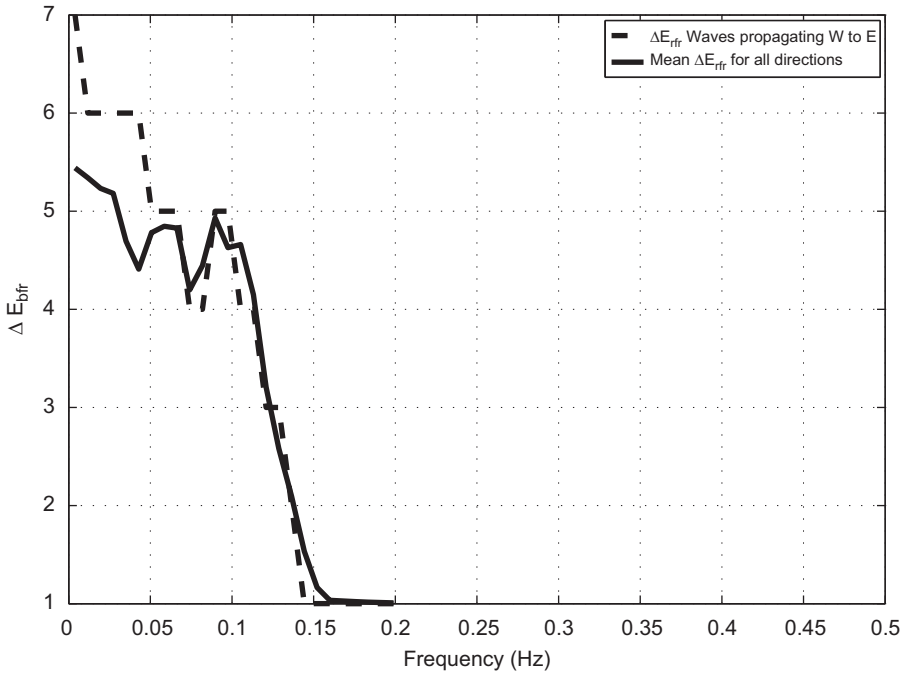

Fig. 16. ΔE_{rfr} values along a line orientated parallel to the wave crests, and level with the most leeward buoy for waves propagating from east to west, and the average for 10 wave directions, (0°,36°,72°,…,324°).

and indicates that the placement of wave sensors can play a critical role in the accuracy of assessment of long-term wave statistics.

When examined for each frequency band in the spectrum, the greatest differences between buoys were observed in the low frequencies, $f < 0.1$ Hz. It is this frequency dependence that increased the bias in the low-order summary parameter, P_t, relative to other parameters.

A small bias was also observed for high frequencies, $f > 0.35$ Hz, although random variability was relatively large. This agrees with observations that the variability in the parameter, T_{m02}, are large relative to the theoretical sampling variability, indicated by variability in the statistic, $Z(T_{m02})$. The conclusion drawn is that a spatial separation introduces an increased random error term, which may be driven by spatial variability in the winds fields, as suggested by Sova and Wyatt (2005), or perhaps tidal flow.

Low frequency waves interact with the local bathymetry in this area, and deterministic spatial differences in wave conditions are likely to contribute to the observed differences. Theoretical calculations of the potential effect of energy dissipation due to bottom friction, and the spatial re-distribution of energy through refraction have been presented. The frequency profile of these two effects are comparable to that of the differences observed in the measured data. This strengthens the hypothesis that these processes could be expected to cause differences in the data measured across the array. The outcome suggests that the rocky protrusion in the seabed situated within the array affects the flow of wave energy between the measurement locations.

The differences observed in the measured data are sufficient to have a significant effect on the wave statistics for the site. Therefore, the seabed and water depth must be a key concern for any wave energy installation, ensuring that physical processes are quantified for an accurate assessment of wave conditions across a site. Published standards for the assessment of wave energy sites suggest the use of wave models to provide a spatial data set of wave data (e.g. Ingram et al., 2011). The results presented in this paper demonstrate that the accuracy of operational wave models at resolving bottom friction and refraction must be considered carefully. Inaccurate, or incomplete formulation of these processes, may lead to significant errors in subsequent assessments.

Interactions with the seabed can be related to observed differences in the low frequencies. However, tidal effects will also be affecting the wave field across the measurement site. Spatial variability in the tidal flows will cause spatial variability in the high frequency measurements and this may be responsible for differences observed in Figs. 6 and 7. Furthermore, bottom dissipation is calculated using the water particle velocity at the seabed. It can therefore be expected that the presence of an ambient current, will affect this process. A detailed assessment of the current field would benefit from an intensive measurement effort to measure the variability of tidal flows, in order to assess their influence on the wave measurements across the array.

When considering causes for the observed differences, one must also consider the operation of the wave sensor. A clear benefit of this facility over previous multipoint deployments (e.g. Allender et al., 1989; Barrett et al., 2009) is that all the sensors are the same, have the same mooring setup, and are time-synchronised. Nevertheless, inaccuracies due to variability in the operation of individual components cannot be ruled out, and a more accurate quantification of the effect of deterministic processes on the wave field at this location would allow a more accurate assessment of the accuracy of the wave sensor. A further deployment of multiple sensors in close proximity in deep water would also achieve the same goal.

7. Conclusions

The direct measurement of a wave field from multiple directional wave buoys provides a high quality data set for the assessment of spatial properties of ocean waves. The site used here is typical of that proposed for full scale wave energy test sites, and the distances considered are relevant to the separations between wave sensors and devices at such sites. The work presented offers a detailed and robust statistical analysis, providing a unique analysis, directly relevant to the assessment of waves for

wave energy sites. The results demonstrate that for WEC deployments, physical processes must be taken into account for an accurate assessment of the wave properties from spatially removed point wave sensors, such as wave buoys. The methodology used is suitable for a comparative assessment of spatial variability where multiple point measurements are available.

References

Allender, J., Audunson, T., Barstow, S.F., Bjerken, S., Krogstad, H.E., Steinbakke, P., Vartdal, L., Borgman, L.E., Graham, C., 1989. The WADIC project: a comprehensive field evaluation of directional wave instrumentation. Ocean Eng. 16 (5–6), 505–536.

Ashton, I.G.C., 2011. Spatial Variability of Wave Fields Over the Scale of a Wave Energy Test Site. Ph.D. Thesis. University of Exeter.

Barrett, S., Ashton, I.G.C., Lewis, T., Smith, G.H., 2009. Spatial & spectral variation of seaways. In: Proceedings of the 8th European Wave and Tidal Energy Conference, 7–10 September 2009, Uppsala, Sweden.

Booij, N., Holthuijsen, L.H., Ris, R.C., 1996. The SWAN wave model for shallow water. In: Proceedings of 24th International Conference on Coastal Engineering, Orlando, vol. 1, pp. 668–678.

Elgar, S., Guza, R., Seymour, R., 1987. Bias of effective degrees of freedom of a spectrum. J. Waterw. Port Coast. Ocean Eng. 7 (2), 93–96.

Goda, Y., 1977. Numerical experiments on statistical variability of ocean waves. Rep. Port Harbour Res. Inst. 16, 3–26.

Goda, Y., 2000. Random Seas and Design of Maritime StructuresWorld Scientific.

Hasselman, K., Barnett, T., Bouws, E., Carlson, H., Cartwright, D., Enke, K., Ewing, J., Gienapp, H., Hasselman, D., Kruesman, P., Meerburg, A., Muller, P., Olbers, D., Richter, K., Sell, W., Walden, H., 1973. Measurements of Wind Wave Growth and Swell Decay during the Joint North Sea Wave Project (JONSWAP). Technical Report. Deutches Hydrographisches Institut, Hamburg.

Holthuijsen, L.H., 2007. Waves in Oceanic and Coastal Waters. Cambridge University Press.

Ingram, D., Smith, G.H., Bittencourt-Ferreira, C., Smith, H.C.M., 2011. Protocols for the Equitable Assessment of Marine Energy Converters. Technical Report, University of Edinburgh. School of Engineering.

Krogstad, H.E., Wolf, J., Thompson, S.P., Wyatt, L.R., 1999. Methods for the intercomparison of wave measurements. Coast. Eng. 37, 235–257.

Mackay, E.B.L., 2009. Wave Energy Resource Assessment. Ph.D. Thesis. University of Southampton, June.

Madsen, O.S., Poon, Y., Graber, H.C., 1988. Spectral wave attenuation by bottom friction: theory. In: Proceedings of the 21st International Conference on Coastal Engineering, vol. 1. ASCE, Torremolinos, pp. 492–504.

Millar, D.L., Smith, H.C.M., Reeve, D.E., 2007. Modelling analysis of the sensitivity of shoreline change to a wave farm. Ocean Eng. 34, 884–901.

Mirfenderesk, H., Young, I.R., 2003. Direct measurements of the bottom friction factor beneath surface gravity waves. Appl. Ocean Res. 25 (5), 269–287.

Mollison, D., 1994. Assessing the wave energy resource. In: Barnett, V., Turkmann, K.F. (Eds.), Statistics for the Environment 2: Water Related Issues. Wiley, pp. 205–221.

NOAA, 2005. Second Workshop Report on the Quality Assurance of Real-time Ocean Data. CCPO Technical Report Series no. 05-01. Accessed on-line at: 〈http://nautilus.baruch.sc.edu/twiki/bin/view〉.

Pitt, E.G., 2009a. Assessment of Wave Energy Resource. Technical Report, EMEC. Accessed on-line at: 〈www.emec.org.uk/standards.asp〉 on 6 December 2011.

Pitt, E.G., 2009b. Assessment of Performance of Wave Energy Conversion Systems. Technical Report, EMEC. Last accessed on-line at: 〈www.emec.org.uk/standards.asp〉 on 6 December 2011.

POL, 2011. Accessed on-line at: 〈www.pol.ac.uk/appl/polpred.html〉 on 6 December.

Pontes, T., 1996. An Atlas of the wave energy resource in Europe. J. Offshore Mech. Arct. Eng. 118, 307–309.

Sanmuganathan, V., 2009. Seawatch Mini II buoy. User Manual. Fugro Oceanor.

Smith, G.H., Taylor, J., 2007. Preliminary Wave Energy Device Performance Protocol. Technical Report. Heriott Watt.

Smith, G.H., Ashton, I.G.C., Evans, M.J., 2008. Spatial variation of wave parameters at site specific scale. In: Proceedings of the 2nd International Conference on Ocean Energy, 15–17 October 2008, Brest, France.

Sova, M., Wyatt, L.R., 2005. Spatial and Temporal Variability in Ocean Wave Measurement. Technical Report. Applied Mathematics Section, University of Sheffield.

Tolman, H.L., 1994. Wind waves and moveable-bed bottom friction. J. Phys. Oceanogr. 24 (5), 994–1009.

Tucker, M.J., 1993. Recommended standard for wave data sampling and near real-time processing. Ocean Eng. 20, 459–474.

Tucker, M.J., Pitt, E.G., 2001. Waves in Ocean Engineering. Vol. 5 of Elsevier Ocean Engineering Book Series. Elsevier.

Young, I.R., 1986. Probability distribution of spectral integrals. J. Waterway Port Coast. Ocean Eng. 112, 338–341.